DOI:
10.1016/j.eml.2024.102246

Document Version
Peer reviewed version

Harnessing centrifugal and Euler forces for tunable buckling of a rotating *elastica*

Eduardo Gutierrez-Prieto[a], Michael Gomez[a,b], Pedro M. Reis[a,*]

[a]*Flexible Structures Laboratory, Institute of Mechanical Engineering, École Polytechnique Fédérale de Lausanne (EPFL), 1015 Lausanne, Switzerland*
[b]*Department of Engineering, King's College London, Strand, London WC2R 2LS, United Kingdom*

Abstract

We investigate the geometrically nonlinear deformation and buckling of a slender elastic beam subject to time-dependent 'fictitious' (non-inertial) forces arising from unsteady rotation. Using a rotary apparatus that accurately imposes an angular acceleration around a fixed axis, we demonstrate that dynamically coupled centrifugal and Euler forces can produce tunable structural deformations. Specifically, by systematically varying the acceleration ramp in a highly automated experimental setup, we show how the buckling onset of a cantilevered beam can be precisely tuned and its deformation direction selected. In a second configuration, we demonstrate that Euler forces can cause a pre-arched beam to snap-through, on demand, between its two stable states. We also formulate a theoretical model rooted in Euler's *elastica* that rationalizes the problem and provides predictions in excellent quantitative agreement with the experimental data. Our findings demonstrate an innovative approach to the programmable actuation of slender rotating structures, where complex loading fields can be produced by controlling a single input parameter, the angular position of a rotating system. The ability to predict and control the buckling behaviors under such non-trivial loading conditions opens avenues for designing devices based on rotational fictitious forces.

Keywords:
Elastic structures, Elastica, Bistable, Fictitious forces, Snap-through

1. Introduction

Nearly every modern machine involves rotary elements [1] (*e.g.,* shafts, wheels, bearings, fans, and turbines), which are so ubiquitous that they often go unnoticed. Since the pioneering stud ies on rotating shafts by Rankine [2], Föppl [3], and Jeffcott [4] over a century ago, predictive modeling has become essential in designing and analyzing rotating machinery. *Rotordynamics* [5–9] has since evolved into a mature field with the primary focus of understanding the vibratory dynamics of rotating structures, to prevent large-amplitude motions that may cause catastrophic failure. Representative examples from the vast literature on rotating structures include improving the operational range and efficiency of machinery, including jet-engine turbines [10], turbo-compressors [11] and hydraulic machines [12], as well as designing centrifugal microfluidic devices [13–15] and novel space structures [16–18].

When formulating Newton's equations of motion in a rotating (non-inertial) frame of reference (FoR), three 'fictitious' body forces appear to act on a rotating body [19]: (i) the *centrifugal* force (proportional to the square of the angular velocity); (ii) the *Coriolis* force (resulting from FoR-body relative motion); and (iii) the *Euler* force (opposing angular acceleration). Unlike bulk elastic media, slender structures may undergo large, global deformations and instabilities under moderate rotational loads, making them well suited to applications in actuation, sensing, and deployable mechanisms [20]. Prior research has investigated rotation-induced instabilities in slender rods [21–24], plates [25–29], and shells [30, 31]. These studies primarily considered the centrifugal forces caused by constant angular velocities, sometimes accompanied by Coriolis forces [32–34], but rarely taking the effects of Euler forces into account: in the presence of angular acceleration, it is necessary to simultaneously consider time-dependent centrifugal forces and other unsteady effects that may be present, significantly complicating analysis. As an exception, motivated by the 'spin-up' of disk drives, the stress distribution and wrinkling of unsteadily rotating elastic disks have been quantified [35, 36].

Here, we perform experiments on unsteadily rotating, slender elastic beams placed eccentrically about a fixed axis (Fig. 1a–c and *Supplementary Material*, Video S1). We also conduct simulations of a dynamic model based on Euler's *elastica* [37], specialized to a rotating FoR. Two configurations are examined: cantilevered beams (clamped-free ends) and beams pre-buckled into a bistable arch (double-clamped). In both cases, the loading arises primarily from centrifugal and Euler forces. For cantilevered beams, beyond a critical angular velocity, the centrifugal force (along $+\mathbf{e}_x$; see Fig. 1 bottom-centre) triggers a buckling instability (Fig. 1d). Simultaneously, the Euler force (along $-\mathbf{e}_y$) acts as a symmetry-breaking 'imperfection' that selects the buckling direction, potentially opposing the beam's natural curvature (Fig. 1e). For arched beams, these forces switch roles: the Euler force drives snap-through buckling while the centrifugal force modulates the asymmetry of the arched shape and the acceleration threshold for instability (Fig. 1f). In both cantilever and arch configurations, we show how combined cen-

*Corresponding author. E-mail address: pedro.reis@epfl.ch (P. M. Reis)

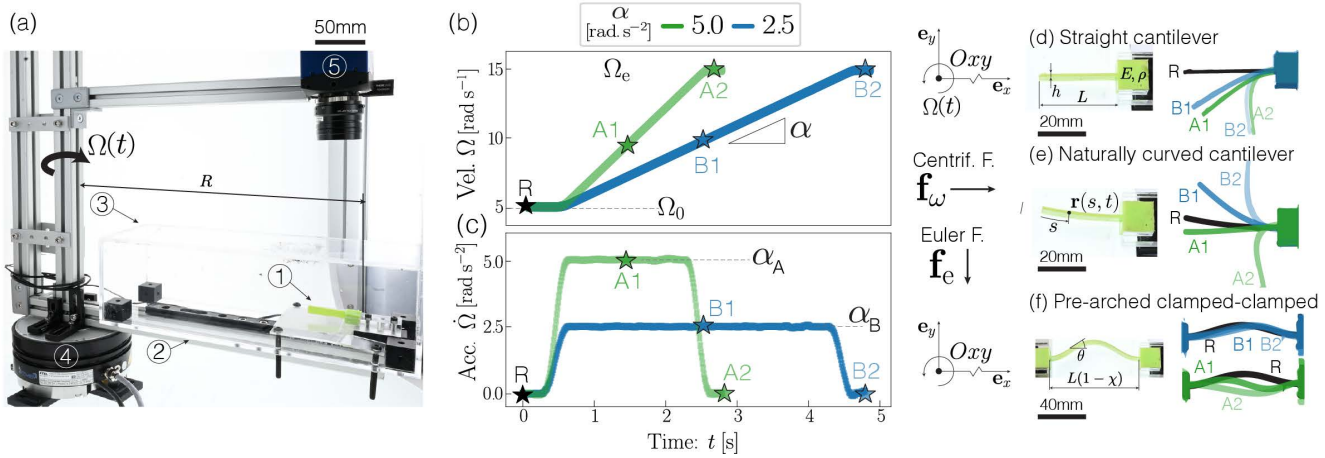

Fig. 1. Elastic beams rotating under controlled angular acceleration. (a) A beam (1) is mounted on a rigid arm (2) inside an acrylic box (3). A torque motor (4) rotates the arm and a camera (5). Right: representative time-series of (b) imposed angular velocity, $\Omega(t)$, and (c) angular acceleration, $\dot{\Omega}(t)$, with $\alpha = \{2.5, 5\}\,\mathrm{rad\,s^{-2}}$ (blue/green curves; see legend) and $(\Omega_0, \Omega_e) = (5, 15)\,\mathrm{rad\,s^{-1}}$. Bottom panels: undeformed (top row) and deformed (lower row) specimens for (d) straight and (e) naturally-curved cantilevers; and (f) pre-arched (double-clamped) beam. Deformed configurations are taken at the instances labeled in panels (b, c). See also *Supplementary Material*, Videos S1–S3.

trifugal and Euler forces cause a subtle interplay between dynamic and symmetry-breaking structural effects, which can be rationalized and precisely controlled. Our study highlights how unsteady rotational loads can be leveraged for function in a new class of tunable mechanisms.

2. Experiments with controlled acceleration ramps

We perform experiments on beams cast from vinyl polysiloxane (VPS, Elite Double, Zhermack), a silicone-based elastomer: for the cantilevered beams we use VPS32 (Young's modulus $E = 1.164\,\mathrm{MPa}$, density $\rho = 1170\,\mathrm{kg\,m^{-3}}$), while for the pre-arched beams we use VPS22 ($E = 863\,\mathrm{kPa}$, $\rho = 1190\,\mathrm{kg\,m^{-3}}$) [38, 39]. The casting is achieved using laser-cut acrylic molds to yield uniform, rectangular beams of width $b = 10\,\mathrm{mm}$, thickness $h \in [1.8, 2.3]\,\mathrm{mm}$, length $L \in [40, 100]\,\mathrm{mm}$ and (constant) natural curvature $\kappa_0 \in [-5, 5]\,\mathrm{m^{-1}}$. The latter range is only for the cantilevered beams; the arched beams are fabricated with no natural curvature, $\kappa_0 = 0$, prior to clamping. Each specimen is mounted onto a rigid arm attached to a high-torque motor (ETEL RTMBi140-030). An encoder records the angular position of the system at 20 kHz. The beams are clamped in the radial direction $\mathbf{e}_x$, with the outer end at a distance $R \in [350, 700]\,\mathrm{mm}$ from the center of rotation (Fig. 1a). The inner end is either free (cantilevered beams; Figs. 1d, e) or clamped at a distance $L(1-\chi)$ radially inwards from the outer end, where $\chi \in (0, 1)$ (pre-arched beams; Fig. 1f). A digital camera (Mikrotron Eosens mini1, 100–550 fps) mounted onto the rotating FoR records the deformed beams, whose centerlines are extracted via image processing. A transparent box protects each specimen against air drag.

The rotational loading is set by imposing linear ramps of the angular velocity, $\Omega(t)$ (Fig. 1b). These ramps are characterized by the initial angular velocity, Ω_0, and the plateau value α of the angular acceleration, $\dot{\Omega}(t) = \mathrm{d}\Omega/\mathrm{d}t$: we have $\dot{\Omega}(t) = \alpha$ except for short intervals at the start/end of the ramping where $\dot{\Omega}$ varies between 0 and α (Fig. 1c). Additional details on the rotation protocol are provided in Appendix A. The experimental system (motor, encoder, and camera) is fully automated, enabling a systematic exploration of parameters such as angular velocity, acceleration, and jerk.

3. Buckling of unsteadily-rotating cantilevers

First, we perform a series of experiments on rotating, straight ($\kappa_0 = 0$), cantilevered beams (Fig. 1d). The centrifugal force acts along the axis of the undeformed beam ($+\mathbf{e}_x$), exerting a compressive distributed load. Above a critical angular velocity, Ω_c, the beam buckles, causing it to bend abruptly towards $-\mathbf{e}_y$, the direction of the Euler force (Fig. 1d, bottom). When Ω is varied quasi-statically ($\dot{\Omega} \approx 0$), the scenario is analogous to the buckling of a vertical cantilever under increasing self-weight [22, 40, 41]. This gravity-induced buckling is described by a supercritical pitchfork bifurcation [42, 43], as sketched in Fig. 2(a) (solid curve): as the relevant bifurcation parameter increases, the initial (undeformed) state becomes linearly unstable at the bifurcation point where two stable branches of buckled solutions emerge. We anticipate that the buckling in our rotating system also corresponds to a supercritical pitchfork bifurcation at $\Omega = \Omega_c$, but only when $\dot{\Omega} \approx 0$.

For a cantilevered beam rotated with non-negligible angular acceleration $\dot{\Omega}$, which reaches the plateau value of α (Fig. 1c), there are, *a priori*, two possible, opposing effects: (I) Due to dynamic effects, the buckling onset may occur at a *higher* Ω compared to the quasi-static scenario (dashed curve, Fig. 2a). Such delayed bifurcations are typically associated with dynamical systems involving a bifurcation parameter varied at a finite rate [44–46], as is the case with $\Omega(t)$ here. Physically, this delay arises because the system recovers from perturbations over an increasingly long timescale as it approaches the bifurcation point, thus 'lagging' behind its equilibrium value [45]. (II) Alternatively, buckling may occur at a *lower* Ω (dashed-dotted

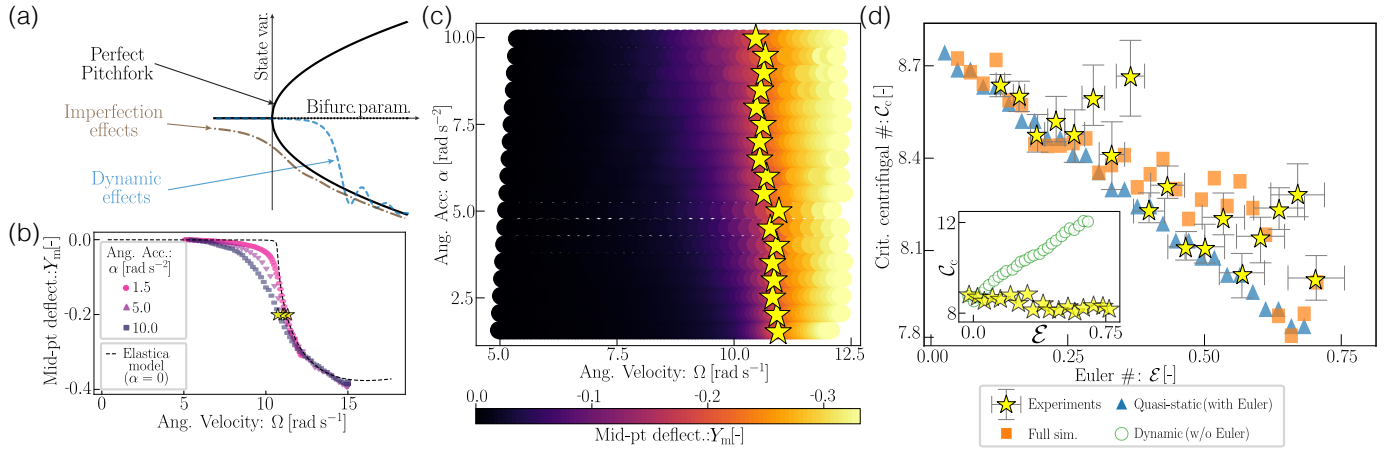

Fig. 2. Buckling of naturally straight, cantilevered beams. (a) Typical response diagrams near a supercritical pitchfork bifurcation. A 'perfect' pitchfork (black curves) is not expected for our system due to either dynamic effects (dashed curve) or symmetry-breaking imperfections (dashed-dotted curve). (b) Normalized midpoint deflection, $Y_m = y_m/L$, obtained experimentally as the angular velocity, Ω, is ramped with acceleration $\alpha = \{1.5,\ 5.0,\ 10.0\}$ rad s^{-2} (symbols; see legend). The dashed curve represents the equilibrium solution of Eqs. (4)–(5). (c) 'Heatmap' of Y_m (see colorbar) vs. Ω and α. Here, and in panel (b), stars indicate the onset of $|Y_m| \geq 0.15$. (d) Critical centrifugal number C_c (onset of $|Y_m| \geq 0.15$) vs. Euler number, $\mathcal{E}$, for experiments and simulations (see legend).

curve, Fig. 2a) due to the asymmetry (or 'imperfection') introduced by the Euler force, similar to how a transverse force (or natural curvature) lowers the buckling onset of a column under self-weight [43]. To discern whether effect (I) or (II) dominates, we vary α in the experiments while fixing all other parameters. In Fig. 2(b), we plot data for the beam's normalized midpoint deflection, $Y_m = y_m/L$, versus the instantaneous angular velocity, Ω, for three different accelerations, $\alpha \in \{1.5, 5.0, 10.0\}$ rad s^{-2}. We find that a higher α decreases the buckling onset and smooths the perfect pitchfork shape, as expected for scenario (II). This behavior is further evidenced in Fig. 2(c), which shows a 'heatmap' of Y_m versus both Ω and α. These results demonstrate that effect (II) prevails: despite the dynamic nature of the loading, the buckling instability is dominated by the symmetry-breaking effect of the Euler force. We will show below that, for cantilevered beams, the loading is quasi-static to a good approximation: the timescale of the loading is slower than the timescale over which oscillations of the beam decay, so that unsteady effects (effect I) are generally negligible.

4. Reduced-order model of a rotating *elastica*

Next, we formulate a geometrically nonlinear model for the elastic deformation of a beam undergoing unsteady rotation and, thus, loaded by fictitious forces. We adopt the *elastica* framework [37], albeit in a rotating FoR, to describe both a cantilevered beam (Fig. 1d–e; experimental results above) and a pre-arched beam (Fig. 1f; discussed below). These two configurations are distinguished by the respective boundary conditions (BCs) applied to the beam's inner end (free or clamped, respectively). We define Cartesian coordinates in the rotating FoR with unit vectors $\{\mathbf{e}_x, \mathbf{e}_y, \mathbf{e}_z\}$, such that the beam's outer end lies on the x-axis; see Fig. 1. Since the beam's dimensions satisfy $h \ll b \ll L$, we assume that the beam undergoes planar (x-y), inextensible, unshearable bending deformations [37]; the strains remain small but with possibly large centerline displacements. The beam is assumed to be in quasi-static moment balance since the rotational inertia of each of its elements is negligible in the limit $h \ll L$ [46].

Under the above assumptions, we represent the deformed centerline in the FoR by $\mathbf{r}(s,t) = x(s,t)\mathbf{e}_x + y(s,t)\mathbf{e}_y$, where the arclength $s \in (0,\ L)$ is measured from the beam's inner end (Fig. 1e). The tangent angle of the centerline, $\theta(s,t)$, is defined by $\mathbf{r}' = \cos\theta\,\mathbf{e}_x + \sin\theta\,\mathbf{e}_y$ (Fig. 1f), where we use $(\cdot)' \equiv \partial(\cdot)/\partial s$ and $\dot{(\cdot)} \equiv \partial(\cdot)/\partial t$. The centrifugal, Euler, and Coriolis forces (per unit length) experienced by the beam are, respectively, $\mathbf{f}_\omega = \rho A\Omega^2\mathbf{r}$, $\mathbf{f}_e = -\rho A\dot{\Omega}\mathbf{e}_z \times \mathbf{r}$, and $\mathbf{f}_c = -2\rho A\Omega\mathbf{e}_z \times (\dot{\mathbf{r}})_r$, where $A = bh$ is the cross-section area and $(\dot{\mathbf{r}})_r = \dot{x}\mathbf{e}_x + \dot{y}\mathbf{e}_y$ is the linear velocity in the rotating FoR; $(\cdot)_r$ denotes differentiation with respect to this frame. Writing $\mathbf{n}(s,t)$ for the resultant force, the dynamic *elastica* equations, expressing conservation of linear and angular momentum with a linearly elastic (Euler-Bernoulli) constitutive law, are [37]:

$$\mathbf{n}' + \mathbf{f}_\omega + \mathbf{f}_e + \mathbf{f}_c = \rho A\,(\ddot{\mathbf{r}})_r + \eta\,(\dot{\mathbf{r}})_r\,, \tag{1}$$

$$B\theta''\mathbf{e}_z + \mathbf{r}' \times \mathbf{n} = \mathbf{0}, \tag{2}$$

where $B = EI$ is the bending modulus, $I = h^3 b/12$ is the area moment of inertia, and we assume isotropic viscous damping (coefficient η), which lumps both external and material effects. The BCs at the outer end are $\mathbf{r}(L,t) = R\mathbf{e}_x$ and $\theta(L,t) = 0$ (Figs. 1d, f). At the inner end, we impose $\mathbf{n}(0,t) = \mathbf{0}$, $\theta'(0,t) = \kappa_0$ (cantilever), or $\mathbf{r}(0,t) = [R - L(1-\chi)]\,\mathbf{e}_x$, $\theta(0,t) = 0$ (arch). The unloaded configurations set the initial conditions.

At this point, we may estimate the relative importance of the different underlying forces (per unit length), noting that the centrifugal force scales as $|\mathbf{f}_\omega| \sim \rho A\Omega^2 R$ and the Euler force as $|\mathbf{f}_e| \sim \rho A\dot{\Omega}R$ (using $|\mathbf{r}| \sim R$). Comparing these two with the typical bending force, $|\mathbf{n}'| \sim B/L^3$, yields the dimensionless quantities:

$$C = \frac{\rho A\Omega^2 R L^3}{B} \quad \text{and} \quad \mathcal{E} = \frac{\rho A\dot{\Omega}RL^3}{B}, \tag{3}$$

which we term the centrifugal and Euler numbers. Similar parameters have been identified in related problems [21, 25–28, 35, 36], albeit with other geometric factors. The timescale of bending motions is $t^* = (\rho A L^4/B)^{1/2}$, obtained from the balance of inertial and bending forces in Eq. (1). Thus, assuming the beam deforms by a distance L over the timescale t^*, the beam velocity scales as $|(\dot{\mathbf{r}})_r| \sim L/t^*$ and the Coriolis force as $|\mathbf{f}_c| \sim \rho A \Omega L/t^*$. Using Eq. (3), we find the ratio $|\mathbf{f}_c|L^3/B = (\delta C)^{1/2}$, where $\delta = L/R$. Because, in general, $C = O(1)$ and $\delta \ll 1$ in our experiments, the Coriolis force is negligible. Alternatively, we note that the typical magnitude of the Coriolis force can be directly compared with the centrifugal force: $|\mathbf{f}_c|/|\mathbf{f}_\omega| \sim |(\dot{\mathbf{r}})_r|/(\Omega R)$. The Coriolis force is, therefore, only significant when the beam's velocity in the FoR is comparable to the tangential velocity of the imposed rotation, which is not the case here due to the small size of the beam.

In what follows, it is advantageous to recast the dynamic elastica equations (Eqs. (1)–(2) and the geometric relation $\mathbf{r}' = \cos\theta\,\mathbf{e}_x + \sin\theta\,\mathbf{e}_y$) as a single equation involving the tangent angle θ only. This process (detailed in the *Supplementary Material*, sections S1.1–S1.2) involves integrating the geometric relation and Eq. (1) to express $\mathbf{r}$ and $\mathbf{n}$ in terms of single and double integrals involving θ, respectively; then substituting these expressions into Eq. (2) and the boundary conditions. In terms of the dimensionless arclength $S = s/L$, time $T = t/t^*$, and force components at the inner end, $\mathbf{n}(0,t) = B/L^2(P\mathbf{e}_x + Q\mathbf{e}_y)$, we obtain the following integro-differential equation for $\theta(S,T)$:

$$0 = \frac{\partial^2\theta}{\partial S^2} - (P - CS)\sin\theta + (Q + \mathcal{E}S)\cos\theta - \int_0^S\int_\xi^1 \left\{\left[\frac{\partial^2\theta}{\partial T^2}(\sigma,T) + \Upsilon\frac{\partial\theta}{\partial T}(\sigma,T) + \delta\mathcal{E}\right]\cos\Delta\theta(S,\sigma,T) + \left[\frac{\partial\theta}{\partial T}(\sigma,T) + (\delta C)^{1/2}\right]^2 \sin\Delta\theta(S,\sigma,T)\right\}\mathrm{d}\sigma\,\mathrm{d}\xi, \quad (4)$$

where we have introduced $\Delta\theta(S,\sigma,T) \equiv \theta(S,T) - \theta(\sigma,T)$ and $\Upsilon = \eta L^4/(Bt^*)$. The BCs become

$$\begin{cases} P = Q = 0, \quad \frac{\partial\theta}{\partial S}(0,T) = \tilde{\kappa}_0, \quad \theta(1,T) = 0 \quad \text{(cantilever)}; \\ \theta(0,T) = \theta(1,T) = 0, \quad \int_0^1 \begin{pmatrix}\cos\theta \\ \sin\theta\end{pmatrix}\mathrm{d}S = \begin{pmatrix}1-\chi \\ 0\end{pmatrix} \quad \text{(arch)}, \end{cases} \quad (5)$$

where $\tilde{\kappa}_0 = L\kappa_0$ is the dimensionless natural curvature of the beam. For arched beams, $P(T)$ and $Q(T)$ are unknown and act as Lagrange multipliers to enforce the integral constraints in Eq. (5).

The main advantage of the integro-differential formulation in Eqs. (4)–(5) is that it is more amenable to reveal the bifurcation structure of the system when working with the single unknown θ (see below). In addition, following previous work [46, 47], the formulation allows for efficient dynamic simulations using the method of lines, in which we discretize the equations in space and integrate the resulting set of ordinary differential equations in time. Since we do not need to explicitly impose the inextensibility of the beam's centerline between each grid point, we avoid a large number of constraints, enabling us to integrate the discretized equations efficiently. The loading is imposed via the time-dependent centrifugal and Euler numbers defined in Eq. (3), evaluated using analytical approximations of the experimental velocity/acceleration profiles (see Appendix C). The other dimensionless parameters fixed in each experiment are the geometric ratio δ and the dimensionless damping coefficient Υ. Further details on the numerical solution are provided in Appendix D.

4.1. Buckling onset: weakly nonlinear analysis

To further investigate the buckling transition observed in cantilevered beams, we perform a weakly nonlinear analysis of equilibrium solutions near the buckling onset, similar to that performed in other buckling problems [48]. We assume a small Euler number, $\mathcal{E} \ll 1$, and small natural curvature, $\tilde{\kappa}_0 \ll 1$, so that the amplitude of the solution before buckling is small: $\theta \ll 1$. We write $C^\star$ for the value of the centrifugal number C at the buckling onset (to be determined). We then perturb [48]

$$C = C^\star + \epsilon C^{(1)} \quad \text{and} \quad \theta = \epsilon^{1/2}\left(\theta^{(0)} + \epsilon\theta^{(1)} + \ldots\right), \quad (6)$$

where $\epsilon \ll 1$ is a fixed parameter (such that $\mathcal{E} = O(\epsilon^{3/2})$ and $\tilde{\kappa}_0 = O(\epsilon^{3/2})$) and $C^{(1)}$ is a control parameter. We substitute the asymptotic expansions into Eqs. (4)–(5) (neglecting time derivatives, and setting $P = Q = 0$ for cantilevered beams) and solve at successive orders in ϵ.

At $O(\epsilon^{1/2})$, we obtain the homogeneous, linear eigenvalue problem for $\theta^{(0)}(S)$ and $C^\star$:

$$\mathcal{L}\theta^{(0)} = 0, \quad \frac{\mathrm{d}\theta^{(0)}}{\mathrm{d}S}(0) = 0, \quad \theta^{(0)}(1) = 0, \quad (7)$$
$$\text{where} \quad \mathcal{L}\theta \equiv \frac{\mathrm{d}^2\theta}{\mathrm{d}S^2} + C^\star\left[S\theta - \delta\int_0^S\int_\xi^1 \Delta\theta(S,\sigma)\,\mathrm{d}\sigma\,\mathrm{d}\xi\right].$$

This determines $\theta^{(0)}$ up to an unknown (scalar) amplitude $A^{(0)}$: we can write $\theta^{(0)} = A^{(0)}\phi^{(0)}$, where $\phi^{(0)}$ satisfies Eq. (7) with normalization $\phi^{(0)}(0) = 1$. In the limit $\delta = L/R \to 0$ applicable to our experimental system, Eq. (7) is equivalent to the classical Greenhill problem for gravitational buckling [40, 42], which can be solved exactly in terms of Airy functions:

$$\phi^{(0)}(S) = \frac{3^{1/6}\Gamma(2/3)}{2}\left[\sqrt{3}\,\mathrm{Ai}\left(-C^{\star\,1/3}S\right) + \mathrm{Bi}\left(-C^{\star\,1/3}S\right)\right]. \quad (8)$$

The remaining boundary condition $\phi^{(0)}(1) = 0$ then yields $\sqrt{3}\,\mathrm{Ai}(-C^{\star\,1/3}) + \mathrm{Bi}(-C^{\star\,1/3}) = 0$, the first positive root of which is $C^\star \approx 7.84$. For non-zero δ, however, the integral term in $\mathcal{L}(\cdot)$ means that an analytical solution to Eq. (7) is generally not possible. We solve the eigenvalue problem numerically (using a shooting method) to determine $\phi^{(0)}(S;\delta)$ and $C^\star(\delta)$; see *Supplementary Material*, section S2.1 for details.

At $O(\epsilon^{3/2})$, Eqs. (4)–(5) yield an inhomogeneous problem of the form (*Supplementary Material*, section S2.2)

$$\mathcal{L}\theta^{(1)} = -\left[(1-\delta)S + \frac{\delta}{2}S^2\right]\epsilon^{-3/2}\mathcal{E} + F\left(C^{(1)}, A^{(0)}, \phi^{(0)}, C^\star\right), \quad \frac{\mathrm{d}\theta^{(1)}}{\mathrm{d}S}(0) = \epsilon^{-3/2}\tilde{\kappa}_0, \quad \theta^{(1)}(1) = 0. \quad (9)$$

Because the homogeneous problem $\mathcal{L}(\cdot) = 0$ has the non-trivial solution $\phi^{(0)}$, the Fredholm Alternative Theorem [49] implies that a solution for $\theta^{(1)}$ exists only if the right-hand side of Eq. (9) satisfies a solvability condition. This solvability condition, which can be formulated by multiplying Eq. (9) by $\phi^{(0)}$ and integrating over $S \in (0, 1)$, yields a cubic equation for the leading-order amplitude $A^{(0)}$:

$$0 = \epsilon^{-3/2}\,(\tilde{\kappa}_0 - c_1\mathcal{E}) - c_2\,C^{(1)}A^{(0)} + c_3{A^{(0)}}^3, \qquad (10)$$

where c_1, c_2, and c_3 are constants that can be expressed in terms of integrals of $\phi_0(S\,;\delta)$ (see *Supplementary Material*, section S2.2).

When $\tilde{\kappa}_0 = 0$ and $\mathcal{E} = 0$, Eq. (10) has the form of an amplitude equation associated with a pitchfork bifurcation [50]: $A^{(0)}(c_2C^{(1)} - c_3{A^{(0)}}^2) = 0$. Since the constants c_2 and c_3 are positive for $\delta \geq 0$ (*Supplementary Material*, Fig. S1), this confirms that the buckling instability is a supercritical pitchfork bifurcation at the critical centrifugal number $C^\star(\delta)$: below the buckling threshold (*i.e.*, $C^{(1)} < 0$) the only (real) solution is $A^{(0)} = 0$, while above the buckling threshold ($C^{(1)} > 0$) the non-zero (real) solutions $A^{(0)} = \pm(c_2C^{(1)}/c_3)^{1/2}$ exist.

4.2. Numerical solution compared with cantilever experiments

The weakly nonlinear analysis above is not valid when the Euler number $\mathcal{E} = O(1)$, or the system is well beyond the buckling onset so that θ is no longer small; in these cases, we must appeal to numerical solutions. For naturally straight, cantilevered beams, Fig. 2(b) shows that the computed post-buckled equilibrium branch (dashed curve) is in excellent agreement with the experiments for small but finite accelerations, serving as validation of the model.

As observed in the experimental results presented in Fig. 2(b), the buckling onset and the ensuing deformation are typically smooth in the presence of imperfections when compared to a perfect pitchfork [50]. Thus, we introduce an empirical definition for the critical centrifugal number, C_c, as the centrifugal number at which the normalized midpoint displacement first exceeds $|Y_m| = 0.15$ (stars in Figs. 2b–d). To further examine the relative importance of the different dynamic effects that are present, we probe the model and decouple the effects resulting from (I) a time-dependent angular velocity and (II) a non-zero Euler force. To do so, we either artificially omit the Euler force in Eq. (4) while keeping a time-dependent angular velocity or, instead, we ignore time-dependence by varying C quasi-statically while maintaining the Euler force. As evidenced by the data in Fig. 2(d), where we plot C_c versus $\mathcal{E}$, the full and quasi-static simulations (squares and triangles, respectively) are in agreement with the experiments (stars). (In Fig. 2(d) and later figures, the Euler number $\mathcal{E}$ is evaluated using Eq. (3) with $\dot{\Omega} = \alpha$, the plateau value of the acceleration during the angular velocity ramp.) By contrast, the simulations with only time-dependence of the angular velocity (circles) deviate significantly from the experiments (see inset). These results further evidence that unsteady effects are negligible compared to the 'imperfection' introduced by the Euler force, *i.e.*, (II) is the relevant scenario.

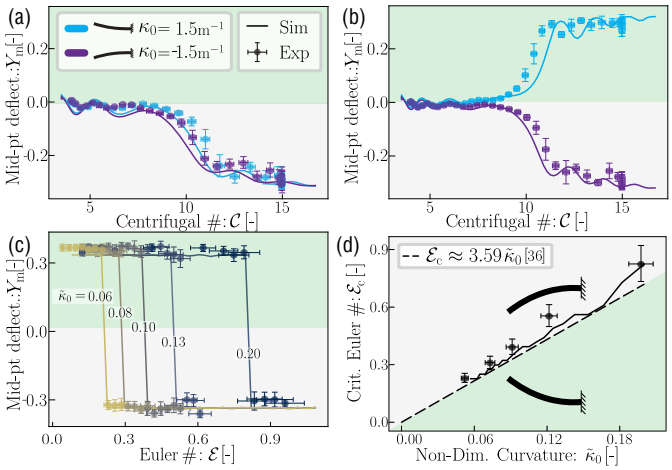

Fig. 3. Buckling of naturally curved, cantilevered beams. (The legend in (a) applies to all panels.) (a, b) Normalized midpoint deflection, $Y_m = y_m/L$, versus the centrifugal number, C, during ramping with Euler number (a) $\mathcal{E} = 0.3$ and (b) $\mathcal{E} = 0.1$. Each panel shows data for two beams with curvatures $\kappa_0 = \pm 1.5\ \text{m}^{-1}$ (purple/blue lines; see legend). See also *Supplementary Material*, Video S2. (c) Post-buckled midpoint deflection, $Y_m|_{C=15}$, versus $\mathcal{E}$ for beams with dimensionless natural curvatures $\tilde{\kappa}_0 = \kappa_0/L \in \{0.06, 0.08, 0.1, 0.13, 0.2\}$. (d) Critical Euler number $\mathcal{E}_c$ (at which the buckling direction is inverted) as a function of $\tilde{\kappa}_0$. Also shown is the predicted boundary, Eq. (11), from the weakly nonlinear stability analysis (dashed line).

Remarkably, despite the dynamic nature of the loading, the quasi-static solution captures the experimental results in Fig. 2(d) nearly as closely as the full dynamic simulations for $\mathcal{E} \lesssim 0.3$ (corresponding to $\alpha \lesssim 3.5\ \text{rad}\,\text{s}^{-2}$). This finding can be rationalized by the following scaling argument. Given an angular acceleration $\dot{\Omega}$, the timescale over which the angular velocity changes appreciably is $\sim \Omega/\dot{\Omega}$. Thus, over a timescale $t \ll \Omega/\dot{\Omega}$, the variation of Ω is negligible and Ω can be considered constant. Meanwhile, oscillations of the beam will decay sufficiently for times $t \gg [t]_d$, where $[t]_d = 2\rho A/\eta$ is the decay timescale of small-amplitude underdamped oscillations [51]. Combining these two observations, we expect that the beam is in quasi-static equilibrium for each Ω provided $\rho A/\eta \ll \Omega/\dot{\Omega}$ (or $\Upsilon^{-1} \ll \delta^{-1/2}C^{1/2}\mathcal{E}^{-1}$ in dimensionless terms). For accelerations $\dot{\Omega} = \alpha \lesssim 3.5\ \text{rad}\,\text{s}^{-2}$, using $\Omega \sim 10\ \text{rad}\,\text{s}^{-1}$ (the typical value at the buckling onset; see Fig. 2c) and $\eta \approx 0.032$ Pa s for our VPS32 beams (see Appendix B), we find that $\Omega/\dot{\Omega} \gtrsim 2.9$ s and $\rho A/\eta \sim 0.67$ s, so that a quasi-static assumption is reasonable.

A detailed analysis of the midpoint trajectories during ramping indicates the presence of small oscillations due to unsteady effects. In accordance with the scaling argument above, these oscillations are usually small in magnitude so that the numerical curves closely follow the quasi-static solutions. However, the oscillation amplitudes become significant for larger accelerations, causing the discrepancy between the full dynamic simulations and the quasi-static simulations in Fig. 2(d) for $\mathcal{E} \gtrsim 0.3$. We also note that, for pre-arched beams, large oscillations occur and the quasi-static assumption is generally not satisfied due to the much larger accelerations required for snap-through (discussed below).

5. Selecting the buckling direction of curved beams

While for a straight cantilever, the centrifugal load (along $+\mathbf{e}_x$) always buckles the beam in the direction of the Euler force ($-\mathbf{e}_y$), it may be desirable in applications to pre-select the opposite buckling direction ($+\mathbf{e}_y$). This can be achieved by fabricating beams with non-zero natural curvature, κ_0 (Fig. 1e). Fig. 3(a, b) presents experimental results for two such beams possessing equal and opposite non-dimensional natural curvatures, $\tilde{\kappa}_0 = \pm 0.06$, while fixing all other parameters (experimentally, a single beam can be flipped about $\mathbf{e}_x$ before clamping). For large accelerations ($\mathcal{E} = 0.3$ in Fig. 3a; see also panels a–b in Video S2), the two cases are nearly identical, with excellent agreement between experiments and simulations, including the matching of the oscillatory nature of the curves. However, for lower accelerations ($\mathcal{E} = 0.1$ in Fig. 3b; Video S2 panels c–d), the two beams buckle in opposite directions, indicating that the geometric imperfection dominates the transverse Euler force.

To delineate the transition from a curvature-controlled to an (Euler) force-controlled buckling direction, we consider the beam's midpoint displacement, Y_m, at a fixed centrifugal number beyond buckling ($C = 15$): in Fig. 3(c), this is plotted versus $\mathcal{E}$ for five beams with different dimensionless natural curvatures $\tilde{\kappa}_0 = \kappa_0 / L \in [0.06, 0.2]$. As $\tilde{\kappa}_0$ is increased (*i.e.*, increasingly imperfect beams), the transition from buckling along $+\mathbf{e}_y$ (the direction of natural curvature) to $-\mathbf{e}_y$ (the direction of Euler force) occurs at higher values of $\mathcal{E}$, both in experiments (symbols) and simulations (curves). In Fig. 3(d), we plot the critical Euler number, $\mathcal{E}_\mathrm{c}$, for this transition as a function of $\tilde{\kappa}_0$, effectively constructing a phase diagram of the beam's buckling direction. Again, there is excellent agreement between experiments (symbols) and simulations (solid curve). The variations in the solid curve are due to oscillations in the numerical trajectories, which become more pronounced for larger values of the Euler number (recall the discussion at the end of section 4.2); close to the boundary in the phase plane, the buckling direction is highly sensitive to the interaction between these oscillations and the Euler force during ramping when the displacement starts to grow significantly. While centrifugal forces drive the buckling instability of cantilevered beams, for a given $\tilde{\kappa}_0$, the buckling direction can, therefore, be selected on-demand via accurate control of $\mathcal{E}$ according to the phase diagram in Fig. 3(d).

The phase boundary in Fig. 3(d) can also be rationalized using Eq. (10), the amplitude equation obtained from the weakly nonlinear analysis. Eq. (10) indicates that the natural curvature, $\tilde{\kappa}_0$, and Euler number, $\mathcal{E}$, behave analogously to symmetry-breaking imperfections that 'unfold' the perfect pitchfork bifurcation: for $\tilde{\kappa}_0 \neq 0$ or $\mathcal{E} \neq 0$, the amplitude $A^{(0)}$ smoothly varies from zero as C is quasi-statically increased past $C^\star$ (meanwhile, the other buckled solution in the pair $A^{(0)} = \pm(c_2 C^{(1)}/c_3)^{1/2}$ forms a disconnected branch). We can infer the direction of buckling from the sign of the constant term in Eq. (10), namely $\epsilon^{-3/2}(\tilde{\kappa}_0 - c_1 \mathcal{E})$, as this term determines the sign of the amplitude $A^{(0)}$ (since $c_2 > 0$). In particular, the constant term changes sign at the critical Euler number $\mathcal{E}_c = \tilde{\kappa}_0 / c_1$. While, in general, c_1 must be evaluated numerically, in the relevant limit of $\delta \to 0$, we can obtain an analytical expression using the solution for $\phi^{(0)}$ in Eq. (8). We evaluate $c_1 = 3^{-1/3}\Gamma(1/3)^{-1} C^{\star -2/3} \mathrm{Ai}(-C^{\star 1/3})^{-1}$ (*Supplementary Material*, section S2.2) where $C^\star \approx 7.84$, and hence

$$\mathcal{E}_c = 3^{1/3}\Gamma\left(\frac{1}{3}\right) C^{\star 2/3} \mathrm{Ai}\left(-C^{\star 1/3}\right) \tilde{\kappa}_0 \approx 3.59\,\tilde{\kappa}_0. \qquad (11)$$

Eq. (11) is used to plot the phase boundary (dashed line) in Fig. 3(d), which agrees well with the numerical and experimental results despite being formally valid only for $\mathcal{E} \ll 1$.

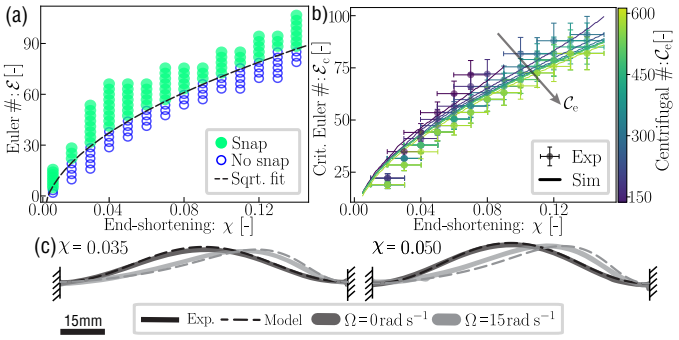

Fig. 4. Snap-through of a pre-arched (double-clamped) beam. (a) Phase diagram for the presence (closed symbols) or absence (open symbols) of snapping in the parameter space of Euler number and end-to-end shortening, $(\mathcal{E}, \chi)$ (here $C_\mathrm{e} = 373$). (b) Beam profiles obtained experimentally and numerically (solid and dashed curves, respectively) for $\chi = 0.035$ (left panel) and $\chi = 0.050$ (right). Shapes are shown at rest (dark gray) and rotating at $\Omega = 15\,\mathrm{rad\,s^{-1}}$ (light gray). (c) Critical Euler number for snapping, $\mathcal{E}_\mathrm{c}$, versus χ at different centrifugal numbers $C_\mathrm{e} \in \{151, 198, 250, 309, 373, 445, 522, 605\}$. See also *Supplementary Material*, Video S3.

6. Acceleration-driven snap-through of a bistable arch

Thus far, for cantilevered beams, we showed that the centrifugal force drives buckling while the Euler force lowers the instability onset. We now turn to the pre-arched beams (Fig. 1f), for which the centrifugal and Euler forces switch roles: the latter drives snapping while the former modulates the instability. In Fig. 4(a), we present a phase diagram for the presence/absence (closed/open symbols) of snapping in the $(\mathcal{E}, \chi)$ parameter space; we fix the final centrifugal number at $C_\mathrm{e} = 373$ ($\Omega_\mathrm{e} = 12\,\mathrm{rad\,s^{-1}}$). As might be expected, the phase boundary above which snapping occurs increases with the end-to-end shortening χ, corresponding to deeper arches. This phase boundary is consistent with the scaling $\mathcal{E} \sim \chi^{1/2}$ (dashed curve); an analogous scaling appears in other snap-through problems involving pre-arched beams [52], and it can be rationalized by comparing the typical midpoint deflection (here due to Euler forces) to the initial arch height. We have thus demonstrated the possibility of actuating rotating mechanisms via the Euler force, whose acting direction can be selected. Euler-actuated mechanisms may switch reversely between stable states, unlike if actuated alone by centrifugal forces, which always act radially outwards.

Although the centrifugal force does not drive snapping, the arch shape becomes increasingly asymmetric when driven at higher angular velocities due to the centrifugal force (Fig. 4c).

Naively, one might expect that this asymmetry would tend to increase the total bending energy, thereby significantly decreasing the energetic barrier for snapping (and hence $\mathcal{E}_c$). In Fig. 4(b) we explore the effect of the centrifugal load, C_e, on the critical Euler number for snapping, $\mathcal{E}_c$, again plotted as a function of end-to-end shortening, χ. Surprisingly, we observe only a modest reduction of $\mathcal{E}_c$ with C_e, in particular for higher values of χ when the shape asymmetry may be large. It is important to note that for the control stability of the motor, we impose loading profiles with finite and constant jerk across experiments (see Appendix A). This imposition places a physical limit on the maximum achievable angular acceleration for a given velocity change. Consequently, at high levels of compression χ, it is generally not possible to generate sufficient Euler forces to induce beam snapping. This physical constraint limits our ability to fully explore the effects of angular velocity in cases with large χ, where one might expect more pronounced effects of shape asymmetry. Overall, these results demonstrate that although the angular velocity does not have a major impact on the critical snap-through load, an accurate angular velocity control can both trigger and modify the snapping of a pre-arched beam.

7. Conclusions

In conclusion, we demonstrated the feasibility of leveraging both centrifugal and Euler forces to precisely trigger and tune, on-demand, instabilities in rotating *elastica* structures by accurately controlling their angular velocity drive. Looking ahead, our investigation can be broadened to include more complex loading profiles (*e.g.*, harmonic velocities), diverse geometries (*e.g.*, tapered beams, plates, and shells), varying material properties (*e.g.*, nonlinear and metamaterial behavior), and different boundary conditions (*e.g.*, pins or roller-springs whose position depends on the centrifugal force). While for our cantilevered beams, we found that the loading is approximately quasi-static, future efforts should address the conditions under which the unsteady effects (effect I) dominate. Even speculatively, we envisage that the understanding developed here will find practical application in a variety of systems involving unsteady rotations, particularly where functionality is achieved through the active actuation of embedded components. Examples include acceleration-actuated operators for centrifugal microfluidic cartridges and automated quality testing of micro-components via complex loading protocols. At larger scales, our insights into the structural effects of Euler forces may contribute to the development of turbines capable of better operating under unsteady regimes and also in aerospace, enabling the design of mechanical switches that are actuated by accelerations encountered during orbital changes. Thus, the advances offered by the present study offer the potential to pave the way for a new class of 'programmable' mechanisms that harness the rich instabilities inherent to unsteadily rotating structures, a novel conceptional framework applicable to generic rotating systems.

Declaration of Competing Interest. The authors declare that they have no known competing financial interests or personal relationships that could have appeared to influence the work reported in this paper.

Declaration of generative AI and AI-assisted technologies in the writing process. During the preparation of this work, the authors used ChatGPT (3.5 & 4) and Grammarly in order to improve the readability and to ensure grammatical correctness of the manuscript. After using this tool/service, the authors reviewed and edited the content as needed and take full responsibility for the content of the published article.

CRediT authorship contribution statement. E. G.-P.: Writing – review & editing, Writing – original draft, Methodology, Investigation, Formal analysis, Conceptualization, Visualization. M. G.: Writing – review & editing, Writing – original draft, Methodology, Investigation, Formal analysis, Software, Validation. P. M. R.: Writing – review & editing, Methodology, Investigation, Formal analysis, Conceptualization, Supervision, Project administration, Funding acquisition, Resources.

Acknowledgments. For the purposes of open access, the author has applied a Creative Commons Attribution (CC BY) licence to any Accepted Author Manuscript version arising from this submission.

Appendix A. Rotation protocol

The rotational loading is set by imposing a time-dependent angular velocity, $\Omega(t)$, in two stages. First, in a pre-loading stage, $\Omega(t)$ is slowly ramped from zero to $\Omega_0 > 0$ at an acceleration $\dot{\Omega} = 5\,\mathrm{rad\,s^{-2}}$, before being held at Ω_0 for 2 s, ensuring the decay of any transient oscillations. Next, in the second loading stage, $\Omega(t)$ is ramped from Ω_0 to Ω_e (where $\Omega_e > \Omega_0$); throughout this stage, the angular acceleration is constant, $\dot{\Omega} = \alpha$, except for short 'jerk intervals' (duration $t_j = 100$ ms) at the start/end of the ramping when $\dot{\Omega}$ rapidly varies between α and zero. Two representative time series of $\Omega(t)$ and $\dot{\Omega}(t)$ are presented in Fig. 1(b) and Fig. 1(c), respectively. The error bars associated with the experimental data are calculated considering the uncertainty of the beam's material properties and geometry, the pixel size and resolution of the imaging system, and uncertainty in the angular position output by the motor encoder. Besides, the error bars of the centrifugal and Euler numbers consider the standard deviation of the measured angular velocity between recorded frames since the temporal resolution of the encoder (20 kHz) is much larger than the recording framerate (100-550 Hz).

Appendix B. Damping coefficient characterization

The value of the damping coefficient η used in our model was measured from underdamped oscillations of the beams (in a cantilevered configuration) in the absence of rotational loading. According to linear stability analysis, small-amplitude underdamped oscillations decay in time like $e^{-t/[t]_d}$, where the time constant is $[t]_d = 2\rho A/\eta$ [51]. Experimentally, we perturbed

the beams and extracted the time series of the tip displacement; the time constant $[t]_d$ was then determined by fitting the envelope of the oscillations. Using the known values of ρ and A (see main text), we obtain $\eta = (0.032 \pm 0.003)$ Pa s and $\eta = (0.043 \pm 0.003)$ Pa s for the beams fabricated using VPS32 and VPS22, respectively.

Appendix C. Rotational loading model

In our dimensionless model, Eqs. (4)–(5), the rotational loading is imposed via the time-dependent centrifugal number, $\mathcal{C}$, and Euler number, $\mathcal{E}$, defined in Eq. (3). To evaluate $\mathcal{C}$ and $\mathcal{E}$, we use analytical expressions for $\Omega(t)$ and $\dot{\Omega}(t)$ that approximate the angular velocity and acceleration imposed experimentally. In particular, we simulate the two dynamic stages (preloading and loading) as described above (Rotation protocol). During the second (loading) stage, we approximate the angular acceleration during each jerk interval using the so-called *smootherstep* function [53], denoted S_2. For a general quantity $a(t)$, this function is a monotonic ramp between the points $(a, t) = (a_0, t_0)$ and (a_1, t_1), with zero first and second-order derivatives at the end-points:

$$S_2(t; t_0, t_1, a_0, a_1) = a_0 + (a_1 - a_0)\left(6\tau^5 - 15\tau^4 + 10\tau^3\right),$$
$$\text{where} \quad \tau = \frac{t - t_0}{t_1 - t_0} \in (0, 1).$$

With Δt denoting the duration of the loading stage (taken to start at $t = 0$), the angular acceleration during the loading stage is modeled as the piece-wise function

$$\dot{\Omega}(t) = \begin{cases} S_2(t; 0, t_j, 0, \alpha) & 0 \le t < t_j, \\ \alpha & t_j \le t < \Delta t - t_j, \\ S_2(t; \Delta t - t_j, \Delta t, \alpha, 0) & \Delta t - t_j \le t < \Delta t. \end{cases}$$

The corresponding angular velocity, $\Omega(t)$, can be determined by integration using the initial condition $\Omega(0) = \Omega_0$. The angular velocity at the end of the loading stage is then $\Omega(\Delta t) = \Omega_0 + \alpha(\Delta t - t_j)$. Thus, to satisfy the imposed final value $\Omega(\Delta t) = \Omega_e$, we choose $\Delta t = (\Omega_e - \Omega_0)/\alpha + t_j$.

Appendix D. Numerical solutions

We define a uniform mesh on $S \in [0, 1]$ with spacing $\Delta S = 1/N$ (so that there are $N + 1$ grid points in total). Our discretization of Eqs. (4)–(5) on this mesh follows that employed previously by Refs. [46, 47] to simulate the snap-through dynamics of an *elastica*. We formulate a scheme with second-order accuracy as $\Delta S \to 0$: we approximate the $\partial^2\theta/\partial S^2$ term in Eq. (4) using a second-order centered difference on the numerical mesh, and we use the trapezium rule to approximate integrals. The resulting system of ODEs is written in matrix-vector form and integrated using the solver `ode15s` in MATLAB. For pre-arched beams, the integral constraints in Eq. (5) mean that the system is differential-algebraic (since the Lagrange multipliers P and Q do not explicitly appear in the integral constraints). This can be avoided using the method described in Ref. [54]: we differentiate the integral constraints twice in time, then eliminate $\partial^2\theta/\partial T^2$ terms (using the discretized form of Eq. (4)) to obtain a closed linear system for P and Q. In all simulations reported in the main text, we take $N = 100$, having checked that the results are insensitive to increasing N or decreasing integration tolerances. Each simulation typically completes in a few seconds on a laptop computer.

At the start of the pre-loading stage, the beam is at rest and in equilibrium in the absence of external loads, $\mathcal{C} = \mathcal{E} = 0$. For cantilevered beams, the beam is stress-free in this equilibrium and everywhere adopts its natural curvature $\tilde{\kappa}_0$, i.e., $\theta(S) = -\tilde{\kappa}_0(1 - S)$. (This may be verified as the equilibrium solution of Eqs. (4)–(5) when $\mathcal{C} = \mathcal{E} = 0$.) In the case of pre-arched beams (with $\tilde{\kappa}_0 = 0$), the beam undergoes Euler (pre-)buckling in the absence of external loads due to the imposed end-to-end shortening, χ, between the double-clamped boundaries. To determine the beam shape, we solve numerically the steady version of Eqs. (4)–(5) (with $\mathcal{C} = \mathcal{E} = 0$). This is achieved by discretizing the equations (in an identical manner to our dynamic simulations) and solving the resulting set of algebraic equations in MATLAB using the routine `fsolve`. As an initial guess, we use the linearized solution for $\theta \ll 1$ corresponding to mode-1 Euler buckling:

$$\theta(S) = 2\chi^{1/2} \sin(2\pi S).$$

References

[1] J. E. Shigley, L. D. Mitchell, H. Saunders, Mechanical Engineering Design (4th Ed.), J. Mech. Transm. Autom. Des. 107 (1985) 145. doi:10.1115/1.3258702.

[2] W. J. M. Rankine, On the centrifugal force of rotating shafts, Engineer 27 (1869) 249.

[3] A. Föppl, Das problem der lavalschen turbinenwelle, Der Civilingenieur 4 (1895) 335–342.

[4] H. H. Jeffcott, The lateral vibration of loaded shafts in the neighbourhood of a whirling speed.—the effect of want of balance, Philos. Mag, 37 (1919) 304–314.

[5] J. S. Rao, History of Rotating Machinery Dynamics, Springer Science & Business Media, Berlin, Germany, 2011.

[6] D. Childs, Turbomachinery Rotordynamics: Phenomena, Modeling, and Analysis, John Wiley & Sons, Hoboken, NJ, 1993.

[7] A. D. Dimarogonas, S. A. Paipetis, T. G. Chondros, Analytical methods in rotor dynamics, Springer Science & Business Media, 2013.

[8] A. Muszynska, Rotordynamics, CRC Press, 2005.

[9] G. Genta, Dynamics of rotating systems, Springer Science & Business Media, 2005.

[10] A. V. Srinivasan, Flutter and Resonant Vibration Characteristics of Engine Blades, J. Eng. Gas Turbines Power. 119 (1997) 742–775. doi:10.1115/1.2817053.

[11] T. Verstraete, Z. Alsalihi, R. A. Van den Braembussche, Multidisciplinary Optimization of a Radial Compressor for Microgas Turbine Applications, J. of Turbomach. 132 (2010). doi:10.1115/1.3144162.

[12] J. Gomes Pereira, E. Vagnoni, A. Favrel, C. Landry, S. Alligné, C. Nicolet, F. Avellan, Prediction of unstable full load conditions in a Francis turbine prototype, Mech. Syst. Signal Process. 169 (2022) 108666. doi:10.1016/j.ymssp.2021.108666.

[13] R. Gorkin, J. Park, J. Siegrist, M. Amasia, B. Seok Lee, J.-M. Park, J. Kim, H. Kim, M. Madou, Y.-K. Cho, Centrifugal microfluidics for biomedical applications, Lab Chip 10 (2010) 1758–1773. doi:10.1039/B924109D.

[14] L. X. Kong, A. Perebikovsky, J. Moebius, L. Kulinsky, M. Madou, Lab-on-a-CD: A Fully Integrated Molecular Diagnostic System, J. Lab. Autom. 21 (2016) 323–355. doi:10.1177/2211068215588456.

[15] M. S. Bhamla, B. Benson, C. Chai, G. Katsikis, A. Johri, M. Prakash, Hand-powered ultralow-cost paper centrifuge, Nat. Biomed. Eng. 1 (2017) 0009.
[16] H. Moravec, A non-synchronous orbital skyhook, J. Astronaut. Sci. 25 (1977) 307–322.
[17] R. Wu, P. C. E. Roberts, C. Soutis, C. Diver, Heliogyro solar sail with self-regulated centrifugal deployment enabled by an origami-inspired morphing reflector, Acta Astronaut. 152 (2018) 242–253. doi:10.1016/j.actaastro.2018.08.012.
[18] M. Gardsback, G. Tibert, Deployment control of spinning space webs, J. Guid. Control Dyn. 32 (2009) 40–50.
[19] P. A. Tipler, G. P. Mosca, Physics for Scientists and Engineers, volume 1, W. H. Freeman and Company, New York, NY, 2002.
[20] P. M. Reis, A Perspective on the Revival of Structural (In)Stability With Novel Opportunities for Function: From Buckliphobia to Buckliphilia, Journal of Applied Mechanics 82 (2015) 111001. doi:10.1115/1.4031456.
[21] N. Mostaghel, I. Tadjbakhsh, Buckling of rotating rods and plates, Int. J. Mech. Sci. 15 (1973) 429–434. doi:10.1016/0020-7403(73)90026-X.
[22] W. F. White, R. G. Kvaternik, K. R. V. Kaza, Buckling of rotating beams, Int. J. Mech. Sci. 21 (1979) 739–745. doi:10.1016/0020-7403(79)90054-7.
[23] I. Aganović, J. Tambača, On the Stability of Rotating Rods and Plates, J. Appl. Math. Mech. 81 (2001) 733–742. doi:10.1002/1521-4001(200111)81:11¡733::AID-ZAMM733¿3.0.CO;2-8.
[24] F. Richard, A. Chakrabarti, B. Audoly, Y. Pomeau, S. Mora, Buckling of a spinning elastic cylinder: linear, weakly nonlinear and post-buckling analyses, Proc. R. Soc. A 474 (2018) 20180242. doi:10.1098/rspa.2018.0242.
[25] J. L. Nowinski, Nonlinear transverse vibrations of a spinning disk, J. Appl. Mech. 31 (1964) 72–78. doi:10.1115/1.3629573.
[26] J.-S. Chen, Y.-Y. Chang, On the unsymmetrical deformation and reverse snapping of a spinning non-flat disk, Int. J. Non-Linear Mech. 42 (2007) 1000–1009.
[27] J.-S. Chen, Y.-Y. Fang, Warping of stationary and rotating heavy disks, Int. J. Solids Struct. 48 (2011) 3032–3040.
[28] M. Delapierre, D. Chakraborty, J. E. Sader, S. Pellegrino, Wrinkling of transversely loaded spinning membranes, Int. J. Solids Struct. 139-140 (2018) 163–173. doi:10.1016/j.ijsolstr.2018.01.031.
[29] C. D. Coman, Wrinkling of a normally loaded, spinning, elastic membrane: An asymptotic approximation, Int. J. Non-Linear Mech. 156 (2023) 104482. doi:10.1016/j.ijnonlinmec.2023.104482.
[30] K. Y. Lam, C. T. Loy, Analysis of rotating laminated cylindrical shells by different thin shell theories, J. Sound Vib. 186 (1995) 23–35. doi:10.1006/jsvi.1995.0431.
[31] H. Li, K.-Y. Lam, T.-Y. Ng, Rotating Shell Dynamics, Elsevier, Amsterdam, Netherlands, 2005.
[32] S. P. Sane, A. Dieudonné, M. A. Willis, T. L. Daniel, Antennal Mechanosensors Mediate Flight Control in Moths, Science 315 (2007) 863–866. doi:10.1126/science.1133598.
[33] S. Sreenivasamurthy, V. Ramamurti, Coriolis effect on the vibration of flat rotating low aspect ratio cantilever plates, J. Strain Anal. Eng. Des. 16 (1981) 97–106. doi:10.1243/03093247V162097.
[34] J. R. Banerjee, D. Kennedy, Dynamic stiffness method for inplane free vibration of rotating beams including Coriolis effects, J. Sound Vib. 333 (2014) 7299–7312. doi:10.1016/j.jsv.2014.08.019.
[35] S. Tang, Note on acceleration stress in a rotating disk, Int. J. Mech. Sci. 12 (1970) 205–207. doi:10.1016/0020-7403(70)90020-2.
[36] J. E. Sader, M. Delapierre, S. Pellegrino, Shear-induced buckling of a thin elastic disk undergoing spin-up, Int. J. Solids Struct. 166 (2019) 75–82. doi:10.1016/j.ijsolstr.2019.01.038.
[37] B. Audoly, Y. Pomeau, Elasticity and Geometry: From Hair Curls to the Non-linear Response of Shells, Oxford University Press, Oxford, UK, 2010.
[38] P. Grandgeorge, T. G. Sano, P. M. Reis, An elastic rod in frictional contact with a rigid cylinder, J. Mech. Phys. Solids 164 (2022) 104885. doi:10.1016/j.jmps.2022.104885.
[39] P. Leroy-Calatayud, M. Pezzulla, A. Keiser, K. Mulleners, P. M. Reis, Tapered foils favor traveling-wave kinematics to enhance the performance of flapping propulsion, Phys. Rev. Fluids 7 (2022) 074403. doi:10.1103/PhysRevFluids.7.074403.
[40] M. A. Greenhill, Determination of the greatest height consistent with stability that a vertical pole or mast can be made, and of the greatest height to which a tree of given proportions can grow, Camb. Phil. Soc. Proc. 4 (1881) 65–73.
[41] J. M. T. Thompson, On the simulation of a gravitational field by a centrifugal field, Int. J. Mech. Sci. 13 (1971) 979–986.
[42] C. Y. Wang, A critical review of the heavy elastica, Int. J. Mech. Sci. 28 (1986) 549–559.
[43] L. N. Virgin, R. H. Plaut, Postbuckling and vibration of linearly elastic and softening columns under self-weight, Int. J. Solids Struct. 41 (2004) 4989–5001.
[44] J. Su, The phenomenon of delayed bifurcation and its analyses, in: C. K. R. T. Jones, A. I. Khibnik (Eds.), Multiple-Time-Scale Dynamical Systems, Springer, New York, NY, 2001, pp. 203–214.
[45] J. R. Tredicce, G. L. Lippi, P. Mandel, B. Charasse, A. Chevalier, B. Picqué, Critical slowing down at a bifurcation, Am. J. Phys. 72 (2004) 799–809.
[46] M. Liu, M. Gomez, D. Vella, Delayed bifurcation in elastic snap-through instabilities, J. Mech. Phys. Solids 151 (2021) 104386.
[47] M. Gomez, Ghosts and bottlenecks in elastic snap-through, Ph.D. thesis, University of Oxford, 2018.
[48] P. Howell, G. Kozyreff, J. Ockendon, Applied Solid Mechanics, Cambridge University Press, Cambridge, UK, 2009.
[49] J. P. Keener, Principles of Applied Mathematics: Transformation and Approximation, CRC Press, Boca Raton, FL, 1988.
[50] S. H. Strogatz, Nonlinear Dynamics and Chaos, Westview Press, Boulder, CO, 2015.
[51] Z. P. Bažant, L. Cedolin, Stability of Structures: Elastic, Inelastic, Fracture and Damage Theories, World Scientific, 2010.
[52] M. Gomez, D. E. Moulton, D. Vella, Passive control of viscous flow via elastic snap-through, Phys. Rev. Lett. 119 (2017) 144502.
[53] D. S. Ebert, F. K. Musgrave, D. Peachey, K. Perlin, S. Worley, Texturing & modeling: a procedural approach, Morgan Kaufmann, 2003.
[54] P. T. Ruhoff, E. Præstgaard, J. W. Perram, Efficient algorithms for simulating complex mechanical systems using constraint dynamics, Proc. R. Soc. A 452 (1996) 1139–1165.

Harnessing centrifugal and Euler forces for tunable buckling of a rotating *elastica*
– Supplementary Material –

Eduardo Gutierrez-Prieto[a], Michael Gomez[a,b], Pedro M. Reis[a,*]

[a]*Flexible Structures Laboratory, Institute of Mechanical Engineering, École Polytechnique Fédérale de Lausanne (EPFL), 1015 Lausanne, Switzerland*
[b]*Department of Engineering, King's College London, Strand, London WC2R 2LS, United Kingdom*

In this document, we provide additional information for the calculations presented in the main text. In §S1, we detail the *elastica* model that we use to perform dynamic simulations; in particular, we discuss its formulation in terms of the tangent angle, θ, and its non-dimensionalization. In §S2, we provide further details on the weakly-nonlinear buckling analysis of cantilever beams. Finally, in §S3, we present the captions for the Supplementary Videos S1–S3.

S1. Theoretical formulations

S1.1. Formulation of the elastica *equations in terms of the tangent angle*

Here we show how to recast the dynamic elastica equations (Eqs. (1)–(2) in the main text, together with the geometric relation $\mathbf{r}' = \cos\theta\,\mathbf{e}_x + \sin\theta\,\mathbf{e}_y$) as a single integro-differential equation for the tangent angle, θ. To this end, we reproduce the equations here in component form. Writing $\mathbf{n}(s,t) = n_x(s,t)\mathbf{e}_x + n_y(s,t)\mathbf{e}_y$, and substituting the expressions for the fictitious forces ($\mathbf{f}_\omega = \rho A\Omega^2\mathbf{r}$, $\mathbf{f}_e = -\rho A\dot{\Omega}\mathbf{e}_z \times \mathbf{r}$ and $\mathbf{f}_c = -2\rho A\Omega\mathbf{e}_z \times (\dot{\mathbf{r}})_r$ where $\mathbf{r}(s,t) = x(s,t)\mathbf{e}_x + y(s,t)\mathbf{e}_y$), the dynamic elastica equations become

$$n_x' + \rho A\Omega^2 x + \rho A\dot{\Omega}y + 2\rho A\Omega\dot{y} = \rho A\ddot{x} + \eta\dot{x}, \tag{1}$$

$$n_y' + \rho A\Omega^2 y - \rho A\dot{\Omega}x - 2\rho A\Omega\dot{x} = \rho A\ddot{y} + \eta\dot{y}, \tag{2}$$

$$B\theta'' - n_x\sin\theta + n_y\cos\theta = 0, \tag{3}$$

$$x' = \cos\theta, \quad y' = \sin\theta. \tag{4}$$

Here, as in the main text, we use the shorthand $(\cdot)' \equiv \partial(\cdot)/\partial s$ and $\dot{(\cdot)} \equiv \partial(\cdot)/\partial t$. The boundary conditions (recall the discussion below Eq. (2) in the main text) in component form are

$$x(L,t) = R, \quad y(L,t) = 0, \quad \theta(L,t) = 0 \quad \text{and} \quad \begin{cases} n_x(0,t) = 0, \quad n_y(0,t) = 0, \quad \theta'(0,t) = \kappa_0 & \text{(cantilever);} \\ x(0,t) = R - L(1-\chi), \quad y(0,t) = 0, \quad \theta(0,t) = 0 & \text{(arch).} \end{cases} \tag{5}$$

We first integrate the geometric relations (Eq. (4)) with the boundary conditions $x(L,t) = R$, $y(L,t) = 0$ to obtain

$$x(s,t) = R - \int_s^L \cos\theta(\sigma,t)\,\mathrm{d}\sigma, \quad y(s,t) = -\int_s^L \sin\theta(\sigma,t)\,\mathrm{d}\sigma.$$

Substituting the above expressions into Eqs. (1)–(2), and integrating again with $n_x(0,t) \equiv p(t)$ and $n_y(0,t) \equiv q(T)$ (we do not restrict to the cantilever/pre-arched scenarios for now), we can determine the force resultants as

$$n_x(s,t) = p(t) - \rho A\Omega^2 Rs + \int_0^s\int_\xi^L \left\{\left[\rho A\ddot{\theta}(\sigma,t) + \eta\dot{\theta}(\sigma,t) + \rho A\dot{\Omega}\right]\sin\theta(\sigma,t) + \rho A\left[\dot{\theta}(\sigma,t) + \Omega\right]^2\cos\theta(\sigma,t)\right\}\mathrm{d}\sigma\,\mathrm{d}\xi,$$

$$n_y(s,t) = q(t) + \rho A\dot{\Omega}Rs - \int_0^s\int_\xi^L \left\{\left[\rho A\ddot{\theta}(\sigma,t) + \eta\dot{\theta}(\sigma,t) + \rho A\dot{\Omega}\right]\cos\theta(\sigma,t) - \rho A\left[\dot{\theta}(\sigma,t) + \Omega\right]^2\sin\theta(\sigma,t)\right\}\mathrm{d}\sigma\,\mathrm{d}\xi.$$

*Corresponding author. E-mail address: pedro.reis@epfl.ch (P. M. Reis)

Inserting these expressions into Eq. (3), and making use of the addition formulae for $\sin[\theta(s,t)-\theta(\sigma,t)]$ and $\cos[\theta(s,t)-\theta(\sigma,t)]$, we arrive at

$$0 = B\theta'' - \left(p - \rho A\Omega^2 Rs\right)\sin\theta + \left(q + \rho A\dot{\Omega}Rs\right)\cos\theta - \int_0^s \int_\xi^L \Big\{\left[\rho A\ddot{\theta}(\sigma,t) + \eta\dot{\theta}(\sigma,t) + \rho A\dot{\Omega}\right]\cos\Delta\theta(s,\sigma,t) + \rho A\left[\dot{\theta}(\sigma,t) + \Omega\right]^2 \sin\Delta\theta(s,\sigma,t)\Big\}\mathrm{d}\sigma\,\mathrm{d}\xi, \tag{6}$$

where $\Delta\theta(s,\sigma,t) \equiv \theta(s,t) - \theta(\sigma,t)$. The remaining boundary conditions in Eq. (5) in terms of θ become

$$\begin{cases} p = q = 0, \quad \theta'(0,t) = \kappa_0, \quad \theta(L,t) = 0 \quad \text{(cantilever)}; \\ \theta(0,t) = 0, \quad \theta(L,t) = 0, \quad \int_0^L \cos\theta(s,t)\,\mathrm{d}s = L(1-\chi), \quad \int_0^L \sin\theta(s,t)\,\mathrm{d}s = 0 \quad \text{(arch)}. \end{cases} \tag{7}$$

For arched beams, p and q are (unknown) Lagrange multipliers to enforce the integral constraints in Eq. (7).

S1.2. Non-dimensionalization of the dynamic elastica equations

To non-dimensionalize the problem, it is natural to scale lengths by the beam length, L, time by the inertia-bending timescale, $t^* = (\rho AL^4/B)^{1/2}$, and forces by the typical buckling force, B/L^2. We therefore introduce

$$s = LS, \quad t = t^*T, \quad (p,q) = \frac{B}{L^2}(P,Q).$$

With these re-scalings, and dropping the shorthand $(\cdot)'$ and $\dot{(\cdot)}$ to avoid confusing dimensional/dimensionless derivatives, Eq. (6) becomes (changing dummy variables $\xi \to L\xi$, $\sigma \to L\sigma$ in the integrals)

$$0 = \frac{\partial^2\theta}{\partial S^2} - (P - CS)\sin\theta + (Q + \mathcal{E}S)\cos\theta - \int_0^S \int_\xi^1 \left\{\left[\frac{\partial^2\theta}{\partial T^2}(\sigma,T) + \Upsilon\frac{\partial\theta}{\partial T}(\sigma,T) + \delta\mathcal{E}\right]\cos\Delta\theta(S,\sigma,T) + \left[\frac{\partial\theta}{\partial T}(\sigma,T) + (\delta C)^{1/2}\right]^2 \sin\Delta\theta(S,\sigma,T)\right\}\mathrm{d}\sigma\,\mathrm{d}\xi, \tag{8}$$

where

$$C = \frac{\rho A\Omega^2 RL^3}{B}, \quad \mathcal{E} = \frac{\rho A\dot{\Omega}RL^3}{B}, \quad \delta = \frac{L}{R}, \quad \Upsilon = \frac{\eta L^4}{Bt^*}.$$

We note that $\delta \geq 0$ compares the beam's size, L, to the radial distance, R, and hence measures the relative variation of the fictitious forces along the beam's length.

The boundary conditions (Eq. (7)) become

$$\begin{cases} P = Q = 0, \quad \frac{\partial\theta}{\partial S}(0,T) = \tilde{\kappa}_0, \quad \theta(1,T) = 0 \quad \text{(cantilever)}; \\ \theta(0,T) = 0, \quad \theta(1,T) = 0, \quad \int_0^1 \cos\theta(S,T)\,\mathrm{d}S = 1-\chi, \quad \int_0^1 \sin\theta(S,T)\,\mathrm{d}S = 0 \quad \text{(arch)}, \end{cases} \tag{9}$$

where $\tilde{\kappa}_0 = L\kappa_0$. Equations (8)–(9) are reported as Eqs. (4)–(5) in the main text.

S2. Weakly-nonlinear analysis of buckling of cantilevered beams

In this section, we provide further details on the weakly-nonlinear analysis of the buckling of cantilevered beams. Considering equilibrium solutions, Eqs. (8)–(9) become

$$0 = \frac{\mathrm{d}^2\theta}{\mathrm{d}S^2} + CS\,\sin\theta + \mathcal{E}S\,\cos\theta - \delta\int_0^S\int_\xi^1 \left[\mathcal{E}\cos\Delta\theta(S,\sigma) + C\sin\Delta\theta(S,\sigma)\right]\mathrm{d}\sigma\,\mathrm{d}\xi, \quad \frac{\mathrm{d}\theta}{\mathrm{d}S}(0) = \tilde{\kappa}_0, \quad \theta(1) = 0. \tag{10}$$

As in the main text, we assume that the amplitude of the solution before buckling is small, $|\theta| \ll 1$ (which requires $\mathcal{E} \ll 1$ and $\tilde{\kappa}_0 \ll 1$), and that the system is close to the buckling threshold at the critical centrifugal number $C^\star$, i.e., $|C - C^\star| \ll 1$. We then expand the solution as

$$C = C^\star + \epsilon C^{(1)}, \quad \theta = \epsilon^{1/2}\left(\theta^{(0)} + \epsilon\,\theta^{(1)} + \ldots\right), \tag{11}$$

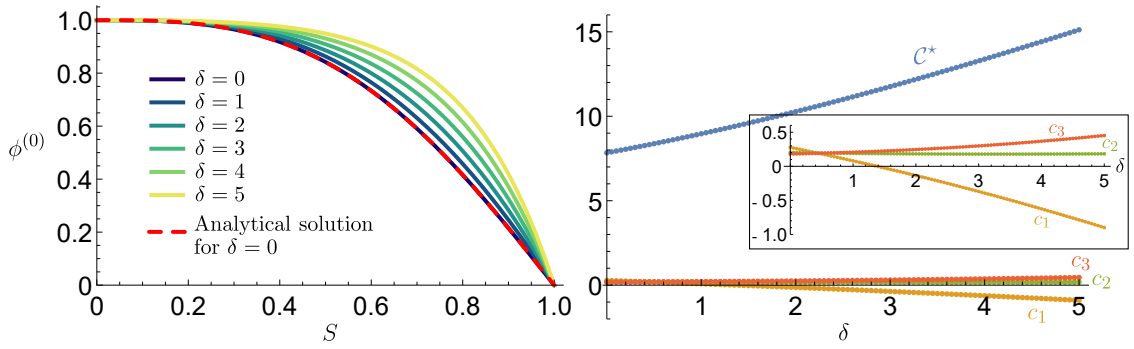

Fig. S1. Solution to the leading-order problem, Eq. (13), obtained numerically by shooting. Left panel: Solution for $\phi^{(0)}(S)$ for different values of δ (see legend), together with the analytical solution (Eq. (14)) for $\delta \to 0$ (red dashed curve). Right panel: Corresponding values of the eigenvalue $C^\star$ and the constants c_1, c_2 and c_3 (defined in Eq. (19)).

where $\epsilon \ll 1$ is a fixed parameter. The asymptotic expansion of θ begins at $O(\epsilon^{1/2})$ because we anticipate a supercritical pitchfork bifurcation, in which the amplitude of the solution grows like the *square root* of the perturbation beyond buckling [1]. In what follows, we assume that $\mathcal{E} = O(\epsilon^{3/2})$ and $\tilde{\kappa}_0 = O(\epsilon^{3/2})$, so that the intrinsic curvature and Euler force only enter the problem at first order, i.e., at $O(\epsilon^{3/2})$. In practice, given $\mathcal{E} \ll 1$ and $\tilde{\kappa}_0 \ll 1$, this can be satisfied by choosing $[\max(\mathcal{E}, \tilde{\kappa}_0)]^{2/3} \lesssim \epsilon \ll 1$.

S2.1. Leading-order problem

At $O(\epsilon^{1/2})$, Eq. (10) yields the homogeneous, linear eigenvalue problem for $\theta^{(0)}$ and $C^\star$:

$$\mathcal{L}\theta^{(0)} = 0, \quad \frac{\mathrm{d}\theta^{(0)}}{\mathrm{d}S}(0) = 0, \quad \theta^{(0)}(1) = 0 \qquad \text{where} \qquad \mathcal{L}\theta \equiv \frac{\mathrm{d}^2\theta}{\mathrm{d}S^2} + C^\star\left[S\theta - \delta\int_0^S\int_\xi^1 \Delta\theta(S,\sigma)\,\mathrm{d}\sigma\,\mathrm{d}\xi\right]. \tag{12}$$

We have $\theta^{(0)} = A^{(0)}\phi^{(0)}$, where $A^{(0)}$ is an unknown (scalar) amplitude and $\phi^{(0)}$ satisfies the eigenvalue problem with normalization condition $\phi^{(0)}(0) = 1$, i.e.,

$$\mathcal{L}\phi^{(0)} = 0, \quad \phi^{(0)}(0) = 1, \quad \frac{\mathrm{d}\phi^{(0)}}{\mathrm{d}S}(0) = 0, \quad \phi^{(0)}(1) = 0. \tag{13}$$

In the limit $\delta \to 0$ (i.e., $L/R \to 0$), the spatial variation of the fictitious forces along the beam length is negligible. The centrifugal force acts analogously to a uniform gravitational field so that the leading-order problem (which only involves the centrifugal force) is equivalent to the classical Greenhill problem for gravitational buckling [2, 3]. In this case, $\mathcal{L}\phi^{(0)} = 0$ reduces to the Airy equation $\mathrm{d}^2\phi^{(0)}/\mathrm{d}S^2 + C^\star S\phi^{(0)} = 0$; the solution of Eq. (13) is

$$\phi^{(0)}(S) = \frac{3^{1/6}\Gamma(2/3)}{2}\left[\sqrt{3}\,\mathrm{Ai}\left(-C^{\star\,1/3}S\right) + \mathrm{Bi}\left(-C^{\star\,1/3}S\right)\right] \qquad \text{where} \qquad \sqrt{3}\,\mathrm{Ai}\left(-C^{\star\,1/3}\right) + \mathrm{Bi}\left(-C^{\star\,1/3}\right) = 0, \tag{14}$$

as reported in Eq. (8) of the main text. The first buckling mode, corresponding to the smallest positive root of the second equation in Eq. (14), occurs at $C^\star \approx 7.84$.

For general δ, we solve Eq. (13) numerically using a shooting method: we solve $\mathcal{L}\phi^{(0)} = 0$ with the boundary conditions at $S = 0$ to determine $\phi^{(0)}(S; C^\star)$, then we impose $\phi^{(0)}(1; C^\star) = 0$ to determine $C^\star$. The shooting is performed in Mathematica [4] using the routines `ParametricNDSolve` and `FindRoot`. Fig. S1 shows the numerically-determined $\phi^{(0)}(S)$ (for the first buckling mode) for several values of $\delta \in [0, 5]$ (left panel), together with the corresponding values of $C^\star(\delta)$ (right panel).

S2.2. First-order problem

At $O(\epsilon^{3/2})$, Eq. (10) becomes

$$\mathcal{L}\theta^{(1)} = -S\left(\epsilon^{-3/2}\mathcal{E} + C^{(1)}\theta^{(0)} - \frac{C^\star}{6}\theta^{(0)^3}\right) + \delta\int_0^S\int_\xi^1\left\{\epsilon^{-3/2}\mathcal{E} + C^{(1)}\Delta\theta^{(0)}(S,\sigma) - \frac{C^\star}{6}\left[\Delta\theta^{(0)}(S,\sigma)\right]^3\right\}\mathrm{d}\sigma\,\mathrm{d}\xi, \quad (15)$$

$$\frac{\mathrm{d}\theta^{(1)}}{\mathrm{d}S}(0) = \epsilon^{-3/2}\tilde{\kappa}_0, \quad \theta^{(1)}(1) = 0, \quad (16)$$

where $\mathcal{L}(\cdot)$ is the same operator defined in the leading-order problem (Eq. (12)). After expanding the integrand in Eq. (15) using $\Delta\theta^{(0)}(S,\sigma) = \theta^{(0)}(S) - \theta^{(0)}(\sigma)$, substituting $\theta^{(0)} = A^{(0)}\phi^{(0)}$, and integrating all terms that are independent of σ, Eq. (15) becomes

$$\begin{aligned}\mathcal{L}\theta^{(1)} = &-\left[(1-\delta)S + \frac{\delta}{2}S^2\right]\epsilon^{-3/2}\mathcal{E} - C^{(1)}\left\{\left[(1-\delta)S + \frac{\delta}{2}S^2\right]\phi^{(0)} - \delta U^{(0)}\right\}A^{(0)}\\ &+ \frac{C^\star}{6}\left\{\left[(1-\delta)S + \frac{\delta}{2}S^2\right]\phi^{(0)^3} - 3\delta\phi^{(0)^2}U^{(0)} + 3\delta\phi^{(0)}V^{(0)} - \delta W^{(0)}\right\}A^{(0)^3}, \end{aligned} \quad (17)$$

where we have introduced the variables

$$U^{(0)}(S) \equiv -\int_0^S\int_\xi^1\phi^{(0)}(\sigma)\,\mathrm{d}\sigma\,\mathrm{d}\xi, \quad V^{(0)}(S) \equiv -\int_0^S\int_\xi^1\left[\phi^{(0)}(\sigma)\right]^2\mathrm{d}\sigma\,\mathrm{d}\xi, \quad W^{(0)}(S) \equiv -\int_0^S\int_\xi^1\left[\phi^{(0)}(\sigma)\right]^3\mathrm{d}\sigma\,\mathrm{d}\xi.$$

Because the homogeneous problem $\mathcal{L}(\cdot) = 0$ has the non-trivial solution $\phi^{(0)}$ (the solution of the leading-order problem, Eq. (13)), the Fredholm Alternative Theorem [5] implies that a solution for $\theta^{(1)}$ exists only if the right-hand side of Eq. (17) satisfies a solvability condition. This solvability condition can be found by multiplying Eq. (17) by $\phi^{(0)}$ and integrating over $S \in (0,1)$. After integrating by parts, making use of Eq. (13) and the boundary conditions in Eq. (16), the terms in $\theta^{(1)}$ vanish and we are left with an equation for the leading-order amplitude $A^{(0)}$ (as reported in Eq. (10) of the main text):

$$0 = \epsilon^{-3/2}\left(\tilde{\kappa}_0 - c_1\mathcal{E}\right) - c_2\,C^{(1)}A^{(0)} + c_3A^{(0)^3}, \quad (18)$$

where we define the constants

$$\begin{aligned}c_1 &= \int_0^1\left[(1-\delta)S + \frac{\delta}{2}S^2\right]\phi^{(0)}(S)\,\mathrm{d}S, \quad c_2 = \int_0^1\left\{\left[(1-\delta)S + \frac{\delta}{2}S^2\right]\left[\phi^{(0)}(S)\right]^2 - \delta U^{(0)}(S)\phi^{(0)}(S)\right\}\mathrm{d}S,\\ c_3 &= \frac{C^\star}{6}\int_0^1\left\{\left[(1-\delta)S + \frac{\delta}{2}S^2\right]\left[\phi^{(0)}(S)\right]^4 - 3\delta U^{(0)}(S)\left[\phi^{(0)}(S)\right]^3 + 3\delta V^{(0)}(S)\left[\phi^{(0)}(S)\right]^2 - \delta W^{(0)}(S)\phi^{(0)}(S)\right\}\mathrm{d}S. \end{aligned} \quad (19)$$

For each δ, these constants are evaluated using the numerical solution for $\phi^{(0)}$; see Fig. S1 (right panel). In addition, in the simplified case $\delta \to 0$, we can obtain an analytical expression for c_1 using the analytical solution for $\phi^{(0)}$ given above (Eq. (14)). Substituting this solution into Eq. (19), and simplifying using standard identities for Airy functions and the fact that $C^\star$ (≈ 7.84) satisfies the eigenvalue equation $\sqrt{3}\,\mathrm{Ai}(-C^{\star\,1/3}) + \mathrm{Bi}(-C^{\star\,1/3}) = 0$, we obtain $c_1 = 3^{-1/3}\Gamma(1/3)^{-1}C^{\star\,-2/3}\mathrm{Ai}(-C^{\star\,1/3})^{-1} \approx 0.278$.

S3. Supplementary Videos

Video S1: Experimental set-up and sample experiment.
This video corresponds to Fig. 1 of the main text, providing a representative example of an experimental run with a pre-arched clamped-clamped beam with a level of compression $\chi = 0.07$. The main panel is imaged in the lab frame, whereas the inset is imaged in the rotating FoR using the camera mounted on the rotating arm. The geometric and material parameters of the beam have been specified in the main text. The rotation drive is characterized by an initial angular velocity $\Omega_0 = 5\,\mathrm{rad/s}$, final angular velocity $\Omega_\mathrm{e} = 15\,\mathrm{rad/s}$, and maximum angular acceleration $\alpha = 70\,\mathrm{rad/s^2}$.

Video S2: Selecting the buckling direction of an intrinsically curved cantilevered beam.
This video corresponds to Fig. 3(a,b) of the main text, providing a view of two naturally-curved cantilevers in the rotating FoR as imaged by the camera mounted on the rotating arm. These beams are rotated with two values of acceleration, $\alpha = \{1.5,\ 10\}\,\mathrm{rad/s^2}$, while fixing the initial angular velocity, $\Omega_0 = 5\,\mathrm{rad/s}$, and the final angular velocity, $\Omega_e = 15\,\mathrm{rad/s}$. The two specimens are fabricated with the same geometry but opposite natural curvature, $\kappa_0 = \pm 1.5\,\mathrm{m^{-1}}$. The other geometric and material properties of the beam have been specified in the main text. Note that the reproduction speed of the videos is different for the two values of acceleration: (a, b) sped-up factor $\times 1.5$ w.r.t. real-time, and (c, d) slowed-up factor $\times 0.3$ w.r.t. real-time.

Video S3: Acceleration-driven snapping of a rotating pre-arched beam .
This video corresponds to Fig. 4(a,b) of the main text, providing a view of pre-arched beams in the rotating FoR as imaged by the camera mounted on the rotating arm. These beams are subject to two values of the end-to-end shortening, $\chi = \{0.07, 0.09\}$, and are rotated with two values of the final angular velocity, $\Omega_e = \{12,\ 15\}\,\mathrm{rad/s^1}$, and different accelerations, α (see legend in the video). The specimen is fabricated according to geometric and material properties specified in the main text.

References

[1] P. Howell, G. Kozyreff, J. Ockendon, Applied Solid Mechanics, Cambridge University Press, Cambridge, UK, 2009.
[2] M. A. Greenhill, Determination of the greatest height consistent with stability that a vertical pole or mast can be made, and of the greatest height to which a tree of given proportions can grow, Camb. Phil. Soc. Proc. 4 (1881) 65–73.
[3] C. Y. Wang, A critical review of the heavy elastica, Int. J. Mech. Sci. 28 (1986) 549–559.
[4] Wolfram Research, Inc., Mathematica, Version 12.1, 2020. Champaign, IL.
[5] J. P. Keener, Principles of Applied Mathematics: Transformation and Approximation, CRC Press, Boca Raton, FL, 1988.